Computational Materials Science 275 (2026) 115098

Contents lists available at ScienceDirect

Computational Materials Science

journal homepage: www.elsevier.com/locate/commatsci

Full length article

Vitriflow: Calibrated amorphous structure ensembles from melt–quench simulations

Jonathon Cottom, Robin Delhomme, Emilia Olsson *

Institute for Theoretical Physics, University of Amsterdam, Science Park 904, Amsterdam, 1098 XH, The Netherlands
Advanced Research Center for Nanolithography, Science Park 106, Amsterdam, 1098 XG, The Netherlands

ARTICLE INFO

Dataset link: https://github.com/Olsson-Materials-Modelling/Vitriflow, 10.5281/zenodo.21111823

Keywords:
Amorphous materials
Melt–quench
Molecular dynamics
Reproducibility
Protocol calibration
Ensemble uncertainty

ABSTRACT

Many structure–property relations in amorphous materials are encoded not only in the mean structure, but in the prevalence, correlations and spatial organisation of minority environments across length scales. Yet atomistic models are commonly validated against bulk averages and a nominal number of structures, without establishing whether the finite population resolves the motifs invoked to explain material behaviour. We present an auditable framework, implemented in the Vitriflow software package, that connects calibrated melt–quench generation to explicit populations and quantity-specific uncertainty. This approach is demonstrated on three distinct benchmark systems. In a-SiO_2, strain is followed from intra-tetrahedral deformation through compressed Si–O–Si bridges to primitive 3-ring topology, showing that the lower angular tail is an organised medium-range population rather than an undifferentiated variation about the network mean. In matched a-Si_3N_4 refinements, DFT redistributes density and first-neighbour length scale, sharpens the force-field first shell and repairs marginal contacts, while the two DFT descendants retain essentially the same first-neighbour topology. In a-Sm_2O_3, the amount and connectivity of partially ordered domains are quantified as they emerge from the disordered parent population, while the mixed coordination characteristic of the amorphous oxide remains robust. Mean structure, distribution tails, inherited topology and connected order are therefore distinct materials variables with distinct uncertainties. There is no universal ensemble size: the Vitriflow package records what was generated, which population was analysed and what that finite population establishes, providing a reproducible route from amorphous structure datasets to quantitatively supported structure–property hypotheses.

1. Introduction

Amorphous materials underpin a wide range of dielectric, optical, electronic, and protective thin-film technologies [1–9]. Their key observables – density, coordination statistics, medium-range topology, defect populations, and the properties derived from them – are structural and cannot be specified by a small unit cell and a set of symmetry labels [10–13]. Atomistic simulation is therefore often required to construct structural models that can be connected directly to diffraction, spectroscopy, transport, interfacial ion migration, and mechanical response [14–18]. At the same time, the absence of long-range periodicity makes amorphous materials intrinsically difficult to model, and a persistent gap separates laboratory structures from the configurations accessible on atomistic time and length scales [19–23].

Among available atomistic routes, melt–quench molecular dynamics is one of the most broadly applicable methods for constructing amorphous models with empirical interatomic potentials, *ab initio* electronic structure forces, or machine-learned interatomic potentials [22,24–30]. For network glasses such as a-SiO_2, it is a plausible proxy for vitrification;[31–33] for non-glass-forming systems, it is better understood as a controlled route to disordered structural models than as a literal representation of synthesis [19–21]. The nominal protocol is simple: heat above the temperature at which initial-packing memory is lost, equilibrate the liquid, cool to the target temperature, and relax. In practice, however, the final amorphous state is path dependent. In silica, cooling rate and system size alter density, coordination, bond-angle distributions, ring statistics, and intermediate-range structural signatures such as the first sharp diffraction peak [15,25,31–37]. In amorphous Si_3N_4 and amorphous Si, both defect content and network topology depend on preparation route and on the chosen interaction model [12,30,38–46].

The ensemble character of amorphous materials is long established [10]; the practical question is the uncertainty carried by one

* Correspondence to: Institute for Theoretical Physics, University of Amsterdam, Science Park 904, Amsterdam, 1098 XH, The Netherlands.
E-mail address: k.i.e.olsson@uva.nl (E. Olsson).

https://doi.org/10.1016/j.commatsci.2026.115098
Received 1 July 2026; Received in revised form 27 August 2026; Accepted 18 September 2026
Available online 27 September 2026
0927-0256/© 2026 The Authors. Published by Elsevier B.V. This is an open access article under the CC BY license (http://creativecommons.org/licenses/by/4.0/).

large cell, a few large cells, or a finite population of independent cell-level sampling units, under a declared population definition and descriptor resolution. Melt temperature, time spent at high temperature, cooling rate, system size, numerical controls, screening criteria, and statistical tolerances are often chosen by convention or computational convenience, while established checks for cooling-rate sensitivity, finite-size effects, liquid stability, ensemble variation, thermostat/barostat behaviour, and neighbour-list handling are seldom linked into one scientific decision chain [31,33,45–54].

Workflow and provenance frameworks such as AiiDA, FireWorks, atomate, signac, and pyiron have substantially improved reproducible execution by standardising automation, recording data lineage, and managing heterogeneous simulation backends [55–60]. Reproducible execution does not, however, establish whether a finite amorphous population resolves the structural quantity used to support a materials conclusion [54]. The missing link is between how structures are generated, which structures or sites define the analysis population, and the uncertainty carried by the resulting estimate. This distinction is increasingly important when amorphous structures are used to train, fine-tune, or benchmark machine-learned interatomic potentials, including foundation models, or when generative models construct candidate populations: a consistently generated dataset may still underresolve the distribution of environments within the chosen descriptor space [61–64].

In this work, we present an auditable framework that links a declared materials question to population construction and quantity-specific uncertainty. It accommodates both prospective generation and retrospective analysis. For a new population, candidate numerical settings can be screened for admissibility and melt–quench choices calibrated within a user-declared protocol family before the resulting population is assessed against a resolution requirement defined by the materials question. For an existing population, the achieved quantity-specific uncertainty and corresponding resolution are reported. The `Vitriflow` software package implements the framework and records the resulting decision chain, distinguishing the available source population from the declared analysis population. It does not replace expert judgement or prescribe a universal protocol, descriptor set, tolerance, or population size; instead, it makes those choices and the scope of the conclusions they support explicit.

We demonstrate this approach on three chemically distinct amorphous systems. The selected oxides and nitride reflect recurring modelling questions across functional amorphous materials, where local motifs and network topology are linked to mechanical evolution, oxygen-ion migration, charge trapping, hydrogen response, oxidation, and charge-induced network transformation [18,65–72]. In a-SiO_2, strain is followed from intra-tetrahedral deformation through compressed Si–O–Si bridges to primitive 3-ring topology, testing whether the lower angular tail forms an organised medium-range population rather than undifferentiated variation about the network mean [10,31,37]. In matched a-Si_3N_4 refinements, the MG2 parent population and its PBE and HSE06 descendants are used to separate changes in density and first-neighbour structure from topology inherited from the common parent [38,39,41]. In a-Sm_2O_3, the prevalence and connectivity of partially ordered regions emerging within a disordered population are quantified, while the robustness of the mixed coordination characteristic of the amorphous oxide is assessed [8,9,73]. Together, these cases show that mean structure, distribution tails, inherited topology, and connected order are distinct materials variables with distinct uncertainty requirements: a population adequate for one quantity need not be adequate for another.

2. Methodological framework

The framework begins with the materials question: which structural quantity is to be estimated, which population it describes, and what precision is required to support the intended conclusion. The `Vitriflow` software package implements the resulting decision chain shown in Fig. 1: numerical preflight, protocol calibration within a user-declared family, population generation where required, structural screening, and quantity-specific statistical analysis. Externally validated settings may enter at the production stage, while an existing population may enter directly at analysis; in the latter case, `Vitriflow` reports the uncertainty achieved by that finite population rather than imposing a population size.

2.1. Material problems and descriptor basis

Amorphous SiO_2, generated from a randomly initialised 192-atom source melt containing 64 Si and 128 O atoms in a cubic cell of side length 21 Å and treated with the SHIK-1 potential [37], tests tetrahedral-network fidelity by separating defect-free silica from oxygen-bridge-defective structures. Amorphous Si_3N_4 tests controlled multi-fidelity refinement: MG2 provides the empirical melt–quench source population, and PBE and HSE06 provide cell-optimised descendants of that same population [41]. Amorphous Sm_2O_3 tests crystal-like screening in an ionic mixed-coordination rare-earth oxide, where fixed-coordination filtering would remove physically relevant local disorder.

For a generated structure or trajectory segment x, the material-specific descriptor map is

$$\Phi(x; D) = \left(d_1(x), d_2(x), \ldots, d_{n_D}(x)\right), \tag{1}$$

where D is the declared descriptor set, d_j is descriptor j, and n_D is the number of descriptors in that set. In these benchmarks, the roles include density, diffusion inferred from mean-squared displacement, radial-distribution peak descriptors, first-shell coordination, bond-angle distributions, ring or topological descriptors, and material-specific local-order metrics. The roles are distinct: descriptors may be used for numerical preflight, protocol calibration, screening, finite-population support, or reporting. They need not be identical across materials or stages and are modular so that they can be adapted to the materials question. The descriptor map and common structural definitions are given in Supplementary Eqs. S6–S14.

2.2. Numerical preflight

Before protocol calibration, the `Vitriflow` package applies a numerical preflight to each user-declared candidate

$$\theta = (\Delta t, \tau_T, \tau_P, s_{\mathrm{skin}}, C_{\mathrm{core}}),$$

where Δt is the timestep, τ_T and τ_P are the thermostat and barostat damping times, s_{skin} is the neighbour-list skin distance, and C_{core} is an optional tabulated C^2 core-splice specification. The preflight rejects gross execution failures and candidates that violate the configured temperature-, pressure-, or volume-control bounds over the declared probe temperatures. The admissibility conditions, ranking score, and Buckingham–ZBL replacement splice are defined in Supplementary Eqs. S15–S24.

The selected setting $\theta^\star$ is the lowest-scoring admissible candidate in the tested domain, with the more conservative barostat damping retained when scores are comparable. This establishes admissibility only within the declared numerical domain; it is not a universal certification of the interaction model, integrator, or timestep. The production timesteps were therefore validated independently using microcanonical (NVE) energy-conservation scans and the number of integration steps in the period associated with the 99th-percentile vibrational-density-of-states wavenumber, as shown in Supplementary Figs. S1 and S2. The selected settings are listed in Table 1 and Supplementary Table S1; complete candidate domains, acceptance criteria, scores, and outcomes are retained in the archived JSON records.

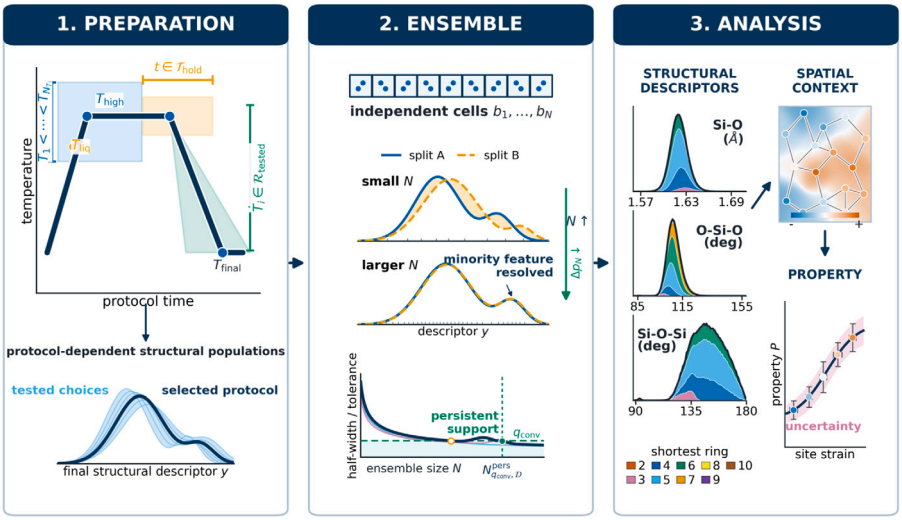


Fig. 1. Decision chain implemented by the `Vitriflow` software package. (1) Preparation: candidate numerical settings and a user-declared protocol family are evaluated, yielding selected settings within the tested domain. (2) Ensemble: independent cells are generated, with the ensemble assessed against a resolution specified by the materials question. (3) Analysis: the source population is screened to define the analysis population, and quantity-specific uncertainty is evaluated. Externally calibrated settings may enter at stage 2, while an existing population may enter directly at stage 3. In the schematic, N is the number of temperature-ladder points, $\mathcal{R}_{\text{tested}}$ is the tested cooling-rate set, and $N^{\text{pers}}_{q_{\text{conv}},D}$ is the persistent crossing size for descriptor y.

Table 1
Selected numerical, protocol, and structural-screen settings used in the three demonstrations. The selected production settings are also reported in Supplementary Table S1; full candidate domains, acceptance criteria, candidate scores, and machine-readable decision records are reported in the archived JSON files. Here, n_{rep} is the calibration-replica count; t_{snap} is the source-snapshot spacing after melt equilibration; $r^{\text{req}}_{\text{in}}$ and $r^{\text{req}}_{\text{out}}$ delimit the requested global C^2 core-splice interval; $\mathcal{A}$ is the ordered tuple of allowed central:neighbour coordinations; r_c is the corresponding first-shell screen cutoff; and $\boldsymbol{\eta}$ is the ordered, dimensionless vector of fractional screen thresholds. Their orders are Si:O/O:Si, Si:N/N:Si, and $(\eta_{\text{cryst}}, \eta_{\text{cluster}})$ for a-SiO_2, a-Si_3N_4, and a-Sm_2O_3, respectively. The a-Si_3N_4 entries are the branch-specific audit cutoffs in MG2/PBE/HSE06 order. The action $\epsilon_s = 1$ excludes a screen-failing cell, whereas $\epsilon_s = 0$ retains it with an audit label.

Quantity	a-SiO_2	a-Si_3N_4	a-Sm_2O_3
Numerical preflight			
Δt (fs)	0.5	1.0	0.5
τ_T (ps)	0.05	0.50	0.10
τ_P (ps)	0.5	5.0	1.0
s_{skin} (Å)	0.25	0.50	1.00
$r^{\text{req}}_{\text{in}}$; $r^{\text{req}}_{\text{out}}$ (Å)	–	–	1.100/1.375
Protocol calibration			
T_{liq} ; T_{high} (K)	4500/5000	3500/4000	3500/4000
n_{rep} (count); $t^{\star}_{\text{melt}}$ (ps)	20; 50.0	20 ; 107.8	20 ; 44.0
t_{snap} (ps)	10	–	–
$\dot{T}^{\star}$ (K ps^{-1})	1.0	1.0	50.0
N (atoms)	192	280	350
Structural screen			
$\mathcal{A}$ (coordination); r_c (Å)	(4, 2) ; 2.07	(4, 3) ; 2.23/2.31/2.29	–
$\boldsymbol{\eta}$	(0, 0)	(0.15, 0.20)	(0.18, 0.12)
ϵ_s	1	0	1

2.3. Protocol calibration

For an admissible numerical setting $\theta^{\star}$, the thermal protocol is

$$p = (T_{\text{high}}, t_{\text{melt}}, \mathcal{S}_T, N), \tag{2}$$

where T_{high} is the high-temperature set point, t_{melt} is the liquid-hold time, $\mathcal{S}_T$ is the user-declared cooling schedule, and N is the number of atoms in the cell. The present demonstrations use linear schedules parameterised by the cooling-rate magnitude $\dot{T}$, but the schedule driver itself is not restricted to this form. Within the user-declared candidate domain $\mathcal{P}(\theta^{\star})$, `Vitriflow` selects

$$p^{\star} = \arg\min_{p \in \mathcal{P}(\theta^{\star})} J(p) \quad \text{subject to} \quad \mathcal{G}_{\text{melt}}, \mathcal{G}_{\text{hold}}, \mathcal{G}_{\text{quench}}, \mathcal{G}_{\text{size}}, \tag{3}$$

where $J(p)$ is the declared computational cost and the four $\mathcal{G}$ terms are the defined melt-window, hold-time, quench-equivalence, and finite-size criteria. Thus $p^{\star}$ is the least-cost passing candidate among the tested choices, not a universal optimum. The selected protocol therefore defines the preparation-conditioned source population only within that tested domain.

The melt-window step identifies the first sustained liquid-like block and sets $T_{\text{high}} = T_{\text{liq}} + \Delta T_{\text{margin}}$, where T_{liq} is the operational liquid onset and ΔT_{margin} is a user-declared temperature margin. Independent replicas then determine the hold-time condition from $\sqrt{\text{MSD}} \geq \alpha_{\text{MSD}} \ell$, where α_{MSD} is the declared displacement fraction and $\ell = (V/N)^{1/3}$ is the characteristic atomic spacing evaluated from the high-temperature cell volume V, together with stationarity tests comparing early and late averages of density and potential energy. Cooling schedules and cell sizes are compared with the slowest or largest tested reference using descriptor-specific equivalence tolerances. The transition score and liquid-state gates are defined in Supplementary Eqs. S28–S38; the hold-time and stationarity conditions in Eqs. S39–S42; and the linear-rate and finite-size comparisons used here in Eqs. S43–S49. The corresponding a-SiO_2, a-Si_3N_4, and a-Sm_2O_3 calibration scans are shown in Supplementary Figs. S3–S5.

2.4. Structural screening and finite-population support

The resulting or imported source population is denoted $\{x_b\}_{b=1}^{N_{\text{gen}}}$. For prospective generation, each x_b is the final relaxed cell associated with one independent cell-level sampling unit, obtained either from an independently seeded trajectory or from a decorrelated source snapshot under the declared material-specific construction; for an existing dataset, the archived cells define the source population directly. Let $\mathcal{S}_{\text{screen}}$ denote the configured set of screens. For $s \in \mathcal{S}_{\text{screen}}$, the package

evaluates the configured descriptor vector

$$\mathbf{d}_{bs} = \Phi_s(x_b; \mathcal{D}_{\text{screen},s}) \tag{4}$$

and stores the label

$$A_{bs} = \mathbf{1}\left[\Psi_s(\mathbf{d}_{bs}) \in \mathcal{I}_s\right], \tag{5}$$

where Ψ_s is the user-declared screen rule and $\mathcal{I}_s$ is its allowed region. Thus $A_{bs} = 1$ denotes a screen-passing cell and $A_{bs} = 0$ an audit-labelled cell. The label does not itself determine exclusion. With $\epsilon_s = 1$ for `exclude=true` and $\epsilon_s = 0$ for `exclude=false`, the post-action mask is

$$R_b = \prod_{s \in \mathcal{S}_{\text{screen}}} \left[A_{bs} + (1 - A_{bs})(1 - \epsilon_s)\right], \tag{6}$$

and the analysis population is

$$\mathcal{E}_{\text{ana}} = \{x_b : R_b = 1\}. \tag{7}$$

The generic scalar, compound, coordination, and crystal-like screen definitions are given in Supplementary Eqs. S50–S60, with the material-specific definitions in Eqs. S77–S92.

For each reported descriptor, the achieved uncertainty is the confidence half-width evaluated on the declared analysis population under its stated independent sampling unit and confidence construction. For scalar descriptor y and a registered population prefix of n independent sampling units, let $\bar{y}_n$ denote the prefix mean, $h_n(y)$ the confidence half-width, and $\tau_y(\bar{y}_n)$ the absolute or relative resolution scale declared for that quantity. The support ratios are

$$R_y(n) = \frac{h_n(y)}{\tau_y(\bar{y}_n)}, \qquad Q(n) = \max_{y \in \mathcal{D}_{\text{conv}}} R_y(n), \tag{8}$$

where $\mathcal{D}_{\text{conv}}$ is the descriptor set relevant to the materials question. The declared support condition is

$$Q(n) \le q_{\text{conv}}, \tag{9}$$

where lower q_{conv} requires a smaller confidence width relative to tolerance and is therefore stricter. The default production target is $q_{\text{conv}} = 0.2$; the descriptor-resolved uncertainty curves are shown in Supplementary Figs. S6–S8; the statistical definitions are given in Supplementary Eqs. S61–S74.

2.5. Stage-resolved diagnostic analysis

Stage-resolved descriptor analysis is used diagnostically to locate when and if protocol-dependent differences enter the melt, liquid-hold, quench, or relaxation trajectory. More closely spaced quench samples are examined near the diffusion-freeze temperature T_f, where the diffusion coefficient D falls below the configured threshold D^* of the same units. The normalised separation and T_f definitions are given in Supplementary Eqs. S75 and S76. Differences already present in the high-temperature liquid indicate incomplete loss of initial-packing memory; differences emerging during cooling implicate the quench schedule; and differences appearing only after cooling implicate low-temperature relaxation or residual-stress effects. These diagnostics do not create an additional acceptance layer.

3. Computational details

The calculations were executed with the `Vitriflow` software package, version v0.4.37.0. Classical molecular dynamics was performed with LAMMPS [74,75]; the DFT-refinement calculations used the electronic-structure backends specified below. The package records the configured inputs, selected protocol, source and analysis populations, screen labels/actions, descriptor tables, support ratios, and provenance. The structural analysis uses the SHIK-1 a-SiO_2, matched MG2/PBE/HSE06 a-Si_3N_4, and Buckingham a-Sm_2O_3 datasets. Atomistic ball-and-stick representations were rendered using the Visualization Toolkit (VTK) [76]. Data plots were generated using Matplotlib [77].

3.1. Classical molecular-dynamics setup

Classical simulations employed periodic boundary conditions and Nosé–Hoover dynamics with isotropic NPT coupling at zero target pressure [47–49,78]. The a-SiO_2 benchmark used the SHIK-1 potential [37], a-Si_3N_4 used the MG2 potential as the empirical baseline [41], and a-Sm_2O_3 used a Coulomb–Buckingham model based on the Sm-containing oxide parameterisation of Olsson et al. [73,79,80] Time steps were selected from the admissible region: 0.5 fs was used for a-SiO_2 and a-Sm_2O_3, while a-Si_3N_4 used 1.0 fs; for a-Sm_2O_3, the divergent Buckingham component was replaced by the tabulated C^2 Buckingham–ZBL splice defined in the Supplementary Information, with the Coulomb contribution unchanged [81]. Temperature scans determined the operational melt window, after which liquid-hold times and quench rates were selected by the descriptor-equivalence criteria defined above. Source populations were constructed from the material-specific independent sampling units until the declared descriptor-support condition was evaluated on the analysis population. For a-Sm_2O_3, the 50 K ps^{-1} production rate was deliberately selected to explore the order–disorder boundary; by contrast, the earlier amorphous-only study used 100 K ps^{-1} to suppress crystal-like fragments [73]. The material-resolved calibration scans and selected settings are reported in Supplementary Figs. S3–S5 and Table S1.

3.2. DFT-refined Si_3N_4 datasets

The MG2+PBE and MG2+HSE06 a-Si_3N_4 datasets were generated by cell optimisation of the MG2-derived amorphous nitride structures at the PBE and HSE06 levels, respectively. These refinements were applied to the MG2-derived structural population rather than obtained from independent DFT melt–quench trajectories.

All DFT calculations were performed spin-polarised using CP2K/Quickstep [82,83]. The PBE branch used the PBE exchange–correlation functional [84]; the HSE06 branch used the HSE06 hybrid functional [85–87] together with the auxiliary density matrix method (ADMM) [88] to reduce the cost of hybrid-functional exchange. DZVP-SR-MOLOPT basis sets [89] were used for valence electrons, and GTH pseudopotentials [90–92] were used for core electrons. The auxiliary plane-wave density cutoff and relative cutoff were set, after convergence testing, to 650 Ry and 70 Ry, respectively, giving an energy precision of approximately 0.1 meV $atom^{-1}$.

Cell optimisations were performed with the BFGS algorithm [93–96]. The convergence criteria were 10^{-7} eV for energy differences and 10^{-3} eV $Å^{-1}$ for forces. After relaxation, the same screen and descriptor pipeline were applied to the MG2, MG2+PBE, and MG2+HSE06 structures.

3.3. Descriptors and comparison metrics

Descriptors were partitioned by role. The preflight and protocol-selection set comprised density, mean-squared-displacement-derived diffusion, simple radial-distribution peak descriptors, and energy stationarity. Final structural analysis was based on total and partial radial distribution functions, bond-angle distributions, coordination statistics evaluated on a fixed cutoff grid, chemically meaningful ring statistics [13], and material-specific artefact metrics. For Sm_2O_3, final comparison emphasised density, pair structure, local-order metrics [97,98], and coordination-distribution stability rather than defect counts against a fixed allowed coordination set. Secondary diagnostics, including structure factors, void measures, and elastic or stress signatures, support the analysis, but do not determine primary acceptance decisions.

Table 2
Material-specific source populations, screen labels/actions, and analysis populations. Counts are N_{gen} : $N_{A=1}$: $N_{A=0}$: N_{ana}, denoting generated, screen-passing, audit-labelled, and analysis cells. Hard screens use `exclude=true`; soft screens use `exclude=false`.

Material	Dataset	Screen	N_{gen} : $N_{A=1}$: $N_{A=0}$: N_{ana}
a-SiO_2	SHIK-1	Exact coordination; hard	2533:1872:661:1872
a-Si_3N_4	MG2	Coordination-outlier; soft	455:420:35:455
a-Si_3N_4	MG2+PBE	Coordination-outlier; soft	455:451:4:455
a-Si_3N_4	MG2+HSE06	Coordination-outlier; soft	455:452:3:455
a-Sm_2O_3	Buckingham	Crystal-like-order; hard	510:430:80:430

4. Results and discussion

Each benchmark defines a different analysis population because each asks a different structural question. In a-SiO_2, exact Si:O = 4 and O:Si = 2 first-shell coordination defines the defect-free analysis population; failed cells form an oxygen-bridge-defective comparison population. In a-Si_3N_4, the coordination-outlier screen uses `exclude=false`: the label is retained as a refinement-response diagnostic, while the full matched MG2-derived population is included in the analysis. In a-Sm_2O_3, the screen targets crystal-like order rather than fixed coordination and excludes labelled cells from the mixed-coordination amorphous analysis population. The common operation is therefore not automatic rejection, but explicit construction of the source population, label, action, analysis population, and claim-support test.

Unless otherwise stated, uncertainties on population means are reported as standard errors over the relevant analysis or audit-labelled population.

4.1. Material-specific screening and ensemble yield

Table 2 summarises the generated populations, screen labels, and analysis populations used in the main-text results. For a-SiO_2, 1872 of 2533 generated SHIK-1 cells satisfy the exact tetrahedral-network criterion, while 661 form an audited oxygen-bridge-defective comparison population. For a-Si_3N_4, the coordination-outlier screen is advisory: all 455 cells in each refinement level are used for descriptor statistics, while 35 MG2, 4 MG2+PBE, and 3 MG2+HSE06 cells carry the high-defect label. This decreasing labelled subset is part of the refinement response. The MG2 ensemble satisfies the short-, medium-, and long-range convergence groups; the PBE and HSE06 descriptors are evaluated on the MG2-derived structures relaxed at each level rather than from independently converged ensembles. For a-Sm_2O_3, the screen retains 430 of 510 generated cells as amorphous and identifies 80 cells as containing significant crystal-like character.

4.2. Tetrahedral-network fidelity in a-SiO_2

Silica provides a stringent test because its average structure is well constrained, while many physically important environments occupy the tails of that structure. An ideal continuous random network consists of fourfold-coordinated Si tetrahedra connected by twofold bridging O atoms [10,16]. These dominant environments determine the radial and angular signatures against which atomistic silica models are commonly assessed. Small rings, compressed Si–O–Si bridges and coordination defects are much less prevalent, but have been associated with strained and potentially active environments in amorphous silica [99,100]. The relevant modelling problem is therefore not only whether a sampled population reproduces silica on average, but whether it resolves the minority structures sufficiently to develop a meaningful structure–property relationship.

The defect-free and defective populations both retain the characteristic tetrahedral-network structure. Their total and partial radial distribution functions are closely matched, and their O–Si–O and Si–O–Si distributions preserve the expected intra- and inter-tetrahedral geometries (Fig. 2; Supplementary Fig. S9). These conventional descriptors establish that both populations represent credible amorphous silica. Their close agreement also exposes the limitation of a mean-structure comparison: minority environments can be distributed differently through the sampled population while remaining weakly expressed in ensemble-averaged pair and angle distributions.

Using the Si–O graph, the exact Si:O = 4 and O:Si = 2 coordination criterion partitions the 2533 generated structures into 1872 defect-free and 661 containing at least one coordination defect. Only 0.408% of O sites are non-ideal, yet such sites occur in 26.10% of the source cells. Local prevalence and population incidence are therefore distinct structural quantities. The deviations are predominantly oxygen-centred, while the tetrahedral Si framework remains largely intact, identifying local rearrangements embedded within an otherwise credible glass network rather than globally collapsed structures. Finally, these coordination defects are understood to originate with the artificially high cooling rate and across the tested cooling rates show a near linear dependence with lower cooling rates producing fewer defective cells albeit at a significantly higher computational cost.

This distinction has a direct modelling consequence. Pooling all atomic sites, or increasing the size of a single model, may improve the estimate of local motif prevalence, but does not determine how that motif is distributed between sampled structures or quantify the uncertainty of its population incidence. A coordination-defect claim must therefore state both its site-level denominator and the population of structures over which it is observed. Full selector attribution and screening sensitivity are reported in Supplementary Figs. S10 and S11, the independent-cell uncertainty analysis is reported in Fig. S6. The 26.10% value is reported as cell incidence across the independent source cells.

Coordination defects are not the only minority environments obscured by conventional average-structure descriptors. Within the coordination-screened population, ring topology organises the tails of the angular distributions. Assigning one shortest zero-winding ring to each exactly twofold O bridge maps the coupled Si–O–Si and O–Si–O geometry across the observed ring classes (Fig. 3a). The sparse 2-ring basin corresponds to edge-sharing tetrahedra, whereas the larger 3-ring population provides a statistically resolved case in which local angular deformation can be related directly to medium-range network topology. The experimental NMR mean and width place the simulated Si–O–Si distribution in a physical reference frame (Fig. 3b). The values 151°, 140° = $\mu - \sigma$ and 129° = $\mu - 2\sigma$ are consequently reference marks, rather than fitted boundaries or discrete structural classes. At 129°, 6.392% of exactly twofold bridges occupy the lower Si–O–Si tail. The complete threshold dependence is important: three-ring association evolves continuously through the distribution and is not created by selecting a single angular cutoff.

Within the 5169 validated primitive 3-rings, reduced inter-tetrahedral Si–O–Si angles are accompanied by a systematic shift in the intra-tetrahedral O–Si–O geometry of the same ring (Fig. 3c). The complete marginal distributions confirm that both angle families are displaced relative to the wider network (Fig. 3d). At the 129° reference, lower-tail Si–O–Si bridges are enriched in primitive 3-rings by a factor of 5.746. The association remains substantial between 129° and 140° and becomes negligible only above approximately 140° (Fig. 3e). The materials consequence is that the lower angular tail is not unstructured statistical variation about the network mean. It is preferentially associated with a defined medium-range topology and coupled to deformation of the O–Si–O geometry within the same ring. Small-ring and compressed-bridge populations may therefore provide a structural basis for interpretations involving strained or active silica environments, although the present analysis establishes structural association rather than a chemical, mechanical or electronic mechanism.

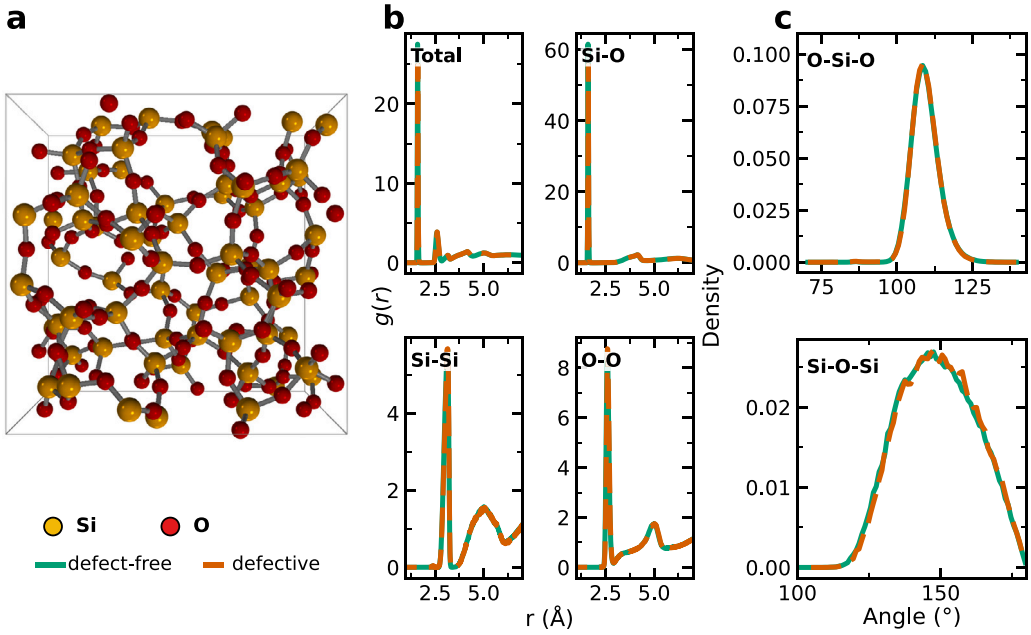


Fig. 2. Structural characterisation of the sampled a-SiO_2 populations. (a) Representative defect-free structure, selected as describing the median density, first-peak, angular-tail and ring-count of the ensemble. Oxygen is shown as red spheres, silicon as yellow spheres and Si–O bonds use a 2.07 Å cutoff. (b) Equal-cell total and partial radial distribution functions for the defect-free and defective populations. (c) Equal-cell O–Si–O and Si–O–Si bond angle distributions.

The modelling consequence is equally direct. A force field or preparation protocol can reproduce density, radial distribution functions and mean bond angles while misrepresenting the population or network context of the tail states relevant to a materials claim. Validation against bulk averages alone is therefore insufficient where the intended inference concerns coordination defects, compressed bridges or small rings. The required test is whether the sampled population resolves the prevalence, incidence and topology of the specific structural quantity being invoked.

These results show that reproducing the mean tetrahedral network does not by itself resolve the minority structures on which tail-based materials interpretations depend. Site prevalence, cell incidence, angular-tail occupancy and ring context are distinct structural quantities, and each carries its own effective uncertainty under the declared population and sampling construction. That uncertainty generally decreases as the sampled population grows, but not at a common rate and not towards a unique population size at which the silica ensemble becomes globally converged. A preparation protocol or force field may therefore support a precise description of the mean network while leaving the prevalence or topology of a relevant tail comparatively uncertain. The appropriate question is not whether the ensemble is "large enough", but what uncertainty has been achieved for the specific structural quantity used and how it relates to the materials question being addressed. The descriptor-resolved uncertainty is reported in Fig. S6, the family- and descriptor-level persistence audits in Tables S2 and S3, and the screening sensitivity in Fig. S11.

4.3. DFT-refinement hierarchy in a-Si_3N_4

The a-Si_3N_4 benchmark addresses a common hierarchy in amorphous materials modelling: structures are generated using a computationally tractable force field and subsequently refined with electronic-structure methods before their properties are evaluated. The unresolved question is what this refinement actually changes. A local DFT optimisation can correct packing, bond lengths and marginal coordination environments, but it cannot be assumed to resample the network topology selected during melt–quench generation. This distinction is important because the electronic, chemical and mechanical response of amorphous nitrides depends on the distribution of local coordination and connectivity, not only on their ensemble-averaged pair structure [38,39,41,66,67,69].

We test this distinction using 455 matched MG2 parent structures, each refined independently along PBE and HSE06 branches. The PBE and HSE06 datasets are therefore paired descendants of the same generated population rather than independent DFT melt–quench ensembles. Atom identity and parent lineage are retained throughout, so structural changes can be evaluated within the same underlying network. Because the branches also differ in their optimisation paths, they are treated as method branches rather than as an unconfounded comparison of exchange–correlation functionals.

The equal-parent radial and angular distributions show that all three branches retain the characteristic heteropolar a-Si_3N_4 network (Fig. 4). Refinement produces visible changes in the first Si–N shell and smaller shifts in the angular distributions, but does not replace the broad network structure inherited from MG2. These descriptors establish the general structural response. They do not, however, distinguish a change in radial scale from a change in distribution shape, or either of these from reconstruction of the first-neighbour graph. Are the changes driven by a sharpening of the neighbour environments at a broadly fixed network topology or is the network being remade?

With `exclude=false`, all 455 matched parents remain in each branch. The audit-labelled highly defective subset decreases from 35 parents for MG2 to 4* for PBE and 3 for HSE06 (Fig. 5a). The asterisk records one PBE parent lying on the registered audit boundary. The reduction in audit labels indicates that DFT refinement removes many of the marginal coordination environments present in the force-field structures.

The largest refinement response is associated with packing and absolute radial scale. Relative to MG2, the PBE density decreases by 2.49%, whereas the HSE06 density differs by only −0.23% (Fig. 5b). The registered Si–N first-peak position shifts by +0.32% for PBE and −0.46% for HSE06, while the mean ring-size and angular changes are smaller. The branches therefore do not respond through one common scalar displacement: cell packing, first-neighbour scale and medium-range descriptors are impacted to differing degrees.

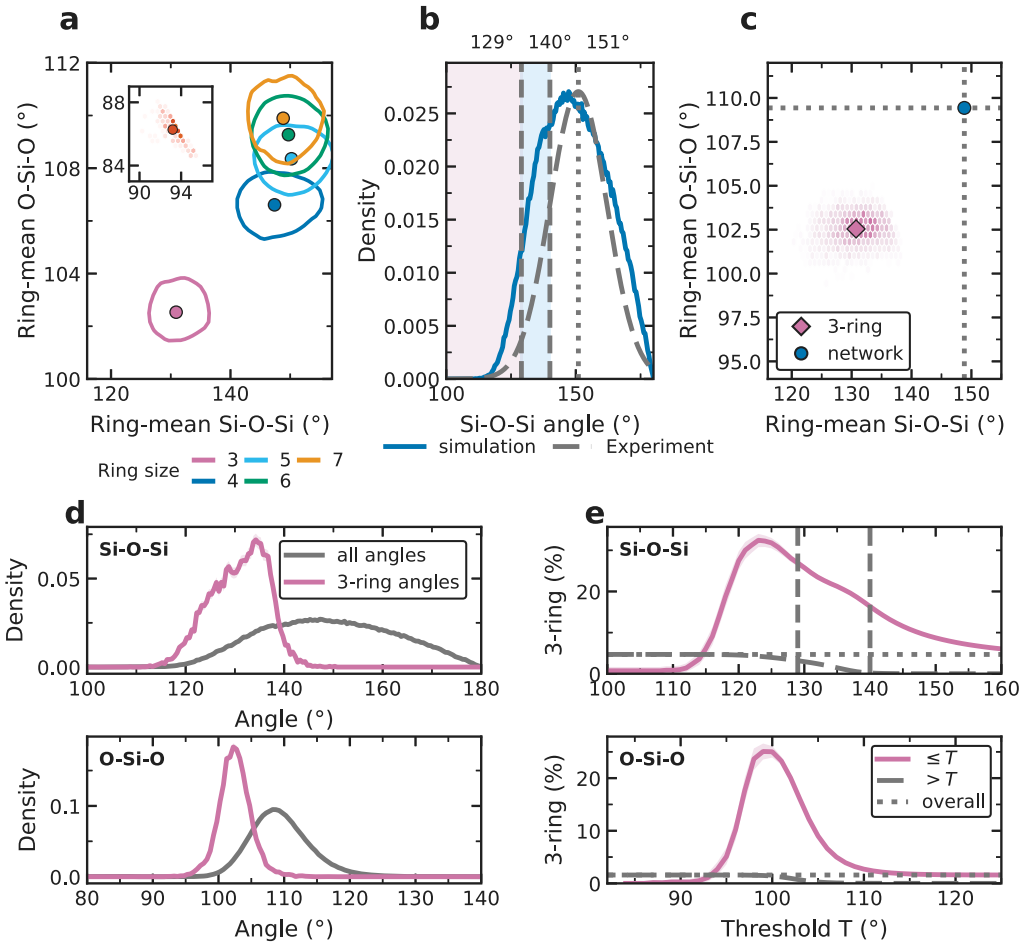


Fig. 3. Ring-resolved Si–O–Si and O–Si–O geometry in amorphous silica. (a) Joint ring-mean angles after assigning one shortest zero-winding ring to each exactly twofold O bridge. Contours show classes 3–7 and the inset resolves the 2-ring basin; this bridge assignment is distinct from the complete primitive-cycle census. (b) Exactly twofold Si–O–Si distribution compared with the NMR-derived normal guide $\mu = 151°$ and $\sigma = 11°$ from Mauri et al. [101]. (c) Joint mean angles for 5169 validated primitive 3-rings. (d) Equal-cell angle distributions for the full network (grey) and 3-rings (pink). (e) Probability of 3-ring membership below (pink) and above (grey dashed) angular threshold T, with the overall probability shown by grey dotted lines.

Both DFT branches nevertheless sharpen the force-field first shell in a closely similar manner. The Si–N peak full width at half maximum decreases from 0.105 Å for MG2 to 0.096 Å for both PBE and HSE06. At the same time, the weight of Si–N pairs lying within 0.05 Å of the registered graph boundary falls from 0.309% for MG2 to 0.219% for PBE and 0.232% for HSE06 (Fig. 5c). The reduction in audit-labelled parents is therefore accompanied by a narrower first shell and fewer pairs whose first-neighbour assignment is sensitive to the graph boundary. DFT refinement primarily repairs marginal force-field environments rather than broadly reordering the network. Referencing each branch to its own first-shell peak separates this metric response from the residual distribution shape (Fig. 5d). After removal of the branch-specific radial displacement, the PBE and HSE06 Si–N distributions are nearly indistinguishable and both remain sharper than MG2. The apparent difference between the two DFT branches in absolute coordinates is dominated by packing and bond-length scale, rather than by substantial differences in first-shell shape.

The graph analysis provides a more stringent topological test. Under the registered common 2.33 Å graph, 84.8% of matched PBE-HSE06 parent pairs have identical first-neighbour edge sets (Fig. 5e). Across the complete population, the PBE-HSE06 edge-union mismatch is only 0.34 edges per 1000 union edges, compared with 16.50 and 16.51 edges per 1000 for MG2-PBE and MG2-HSE06, respectively (Fig. 5f). The mismatch between the two DFT descendants is consequently approximately 49 times smaller than that between either descendant and its MG2 parent. The PBE-HSE06 comparison also contains fewer than 0.2 removed and created edges per parent, whereas each MG2-DFT comparison contains approximately eight.

These results show that DFT refinement changes different levels of the amorphous structure by markedly different amounts. Packing and first-neighbour length scale respond measurably, the force-field first shell sharpens and a small population of marginal contacts is repaired, but the PBE and HSE06 descendants retain nearly identical first-neighbour topology. The two DFT branches therefore converge on essentially the same local network after correcting closely related features of the MG2 population.

The consequence is that structural differences between the PBE and HSE06 branches can be interpreted without conflating them with wholesale reconstruction of the amorphous network. Conversely, the larger MG2-DFT differences include both metric relaxation and local topological repair. This separation is necessary wherever electronic states, trapping sites, chemical response or mechanical transformation are attributed to a specific coordination environment: a change in the electronic-structure description need not imply that a different network population has been sampled.

Each level of this comparison carries a distinct effective uncertainty under the matched-parent sampling construction. Density, first-shell shape, audit-label prevalence and graph mismatch are not resolved to a common precision by one nominal population size. Complete structural distributions and scalar descriptors are reported in Figs. S12 and S13;

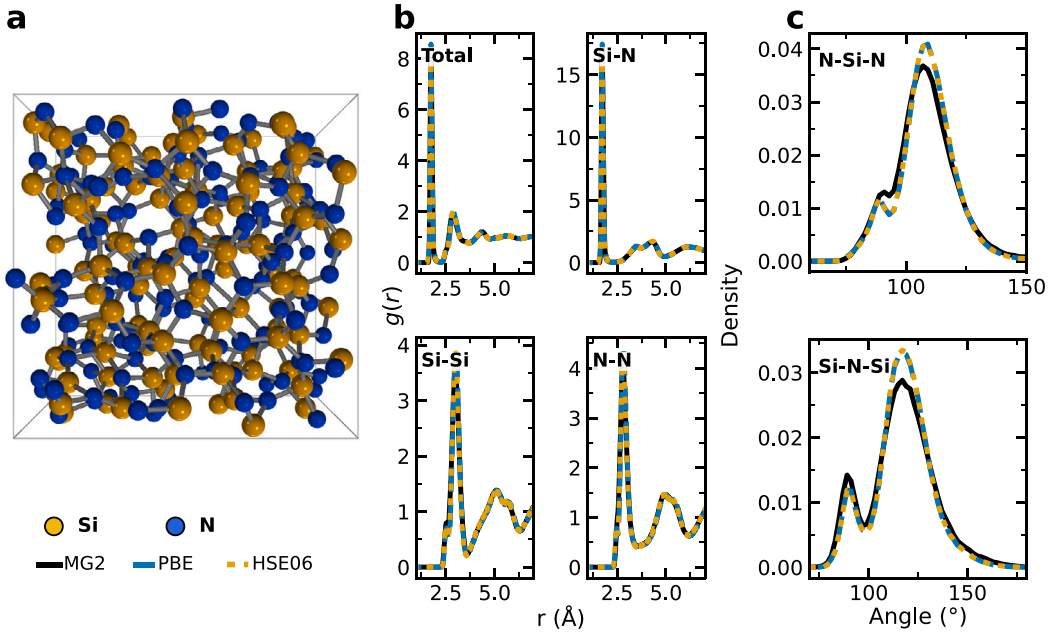


Fig. 4. General structural characterisation of the matched a-Si_3N_4 population. (a) Representative MG2 structure from the matched MG2, PBE and HSE06 parent set. Nitrogen is shown in blue, silicon in yellow and Si–N bonds use a 2.33 Å cutoff. (b) Equal-parent total and partial radial distribution functions for MG2, PBE and HSE06. (c) Equal-parent N–Si–N and Si–N–Si bond angle distributions.

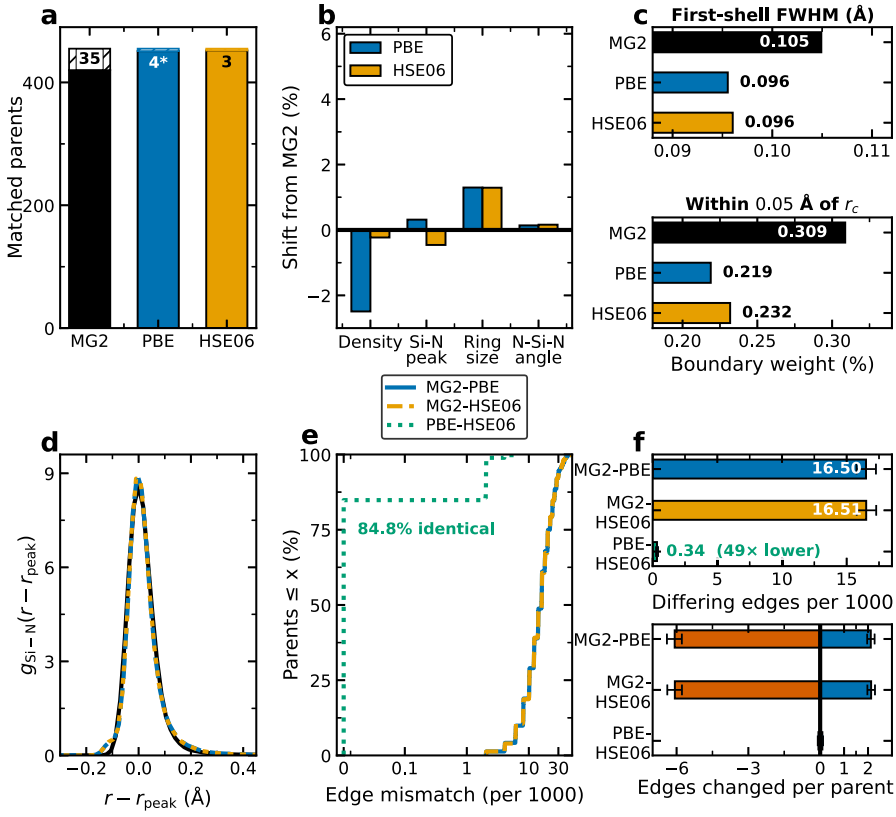


Fig. 5. First-shell sharpening and topology across matched a-Si_3N_4 refinement branches. (a) Matched-parent population and diagnostic audit labels; all 455 parents are retained. The PBE count is 4* because one parent lies on the audit boundary. (b) Relative changes from MG2 in density, Si–N first-peak position, mean ring size and mean N–Si–N angle. (c) Si–N first-shell width and graph-boundary pair weight. (d) Peak-referenced Si–N distributions. In panel c, $r_c = r_c^{\mathrm{RDF},M}$ is the branch-specific registered RDF boundary, distinct from the audit cutoff and the common-topology cutoff; in panel d, $r_{\mathrm{peak}} = r_{\mathrm{pk}}^{(M)}$ is the branch-specific Si–N first-peak position. (e) Common-graph edge mismatch across matched parents; 84.8% of PBE-HSE06 pairs have identical first-neighbour graphs. (f) Aggregate edge mismatch and removed and created edges per parent. PBE and HSE06 are treated as method branches.

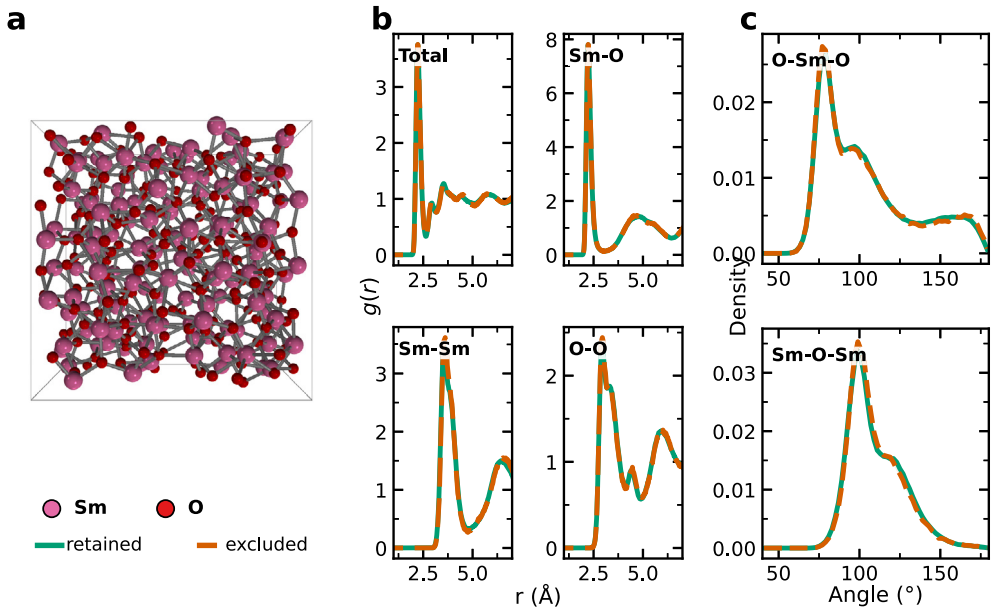


Fig. 6. Structural characterisation of the sampled a-Sm_2O_3 populations. (a) Representative amorphous structure. Oxygen is shown as red spheres, samarium as pink spheres and Sm–O bonds use a 2.95 Å cutoff. (b) Equal-cell total and partial radial distribution functions for the amorphous and partially ordered populations. (c) Equal-cell O–Sm–O and Sm–O–Sm bond angle distributions.

descriptor-resolved uncertainty is shown in Fig. S7; and the separate coordination-audit and graph-boundary sensitivities are reported in Figs. S14 and S15.

4.4. Crystal-like order and mixed coordination in a-Sm_2O_3

Sm_2O_3 poses a different population problem from the Si-based network materials. Broad Sm–O and O–Sm coordination environments are intrinsic to the amorphous rare-earth oxide, so a fixed-coordination screen would remove legitimate local environments and bias the population towards an artificially idealised network [73]. The competing preparation outcome is the formation of extended regions of crystal-like order, which become more prevalent as the cooling schedule allows greater structural ordering. Treating every generated cell as amorphous would therefore mix predominantly disordered structures with partially ordered products, whereas assigning crystallographic phases from a local-order scalar would exceed what the calculation establishes.

This distinction is equally important when melt–quench structures are used to represent partially crystallised or polycrystalline films. Such a description should be supported by a measured prevalence and connectivity of ordered environments, rather than by visual inspection, density or a single order parameter. Here, the screen is consequently used not merely to discard undesirable cells, but to quantify the ordered material generated by the preparation protocol and to construct separate amorphous and partially ordered populations.

The two populations retain the broad pair and angular structure of the disordered Sm–O network, but differ consistently in their short- and medium-range correlations (Fig. 6). The comparison therefore concerns different degrees of order within one chemically related rare-earth-oxide population rather than unrelated structures. It also shows why density or one mean local-order value is insufficient: the relevant distinction is whether ordered sites remain isolated within a disordered network or form an extended connected region.

We identify these environments using the local bond-order construction of Steinhardt and the neighbour-averaged extension of Lechner and Dellago [97,98]. Predominantly amorphous cells have mean crystalline and largest-connected-region fractions $f_{\mathrm{cryst}} = 0.0257 \pm 0.0015$ and $f_{\mathrm{cluster}} = 0.0232 \pm 0.0014$, respectively, whereas the partially ordered population has $f_{\mathrm{cryst}} = f_{\mathrm{cluster}} = 0.348 \pm 0.024$. The near equality of the two values in the partially ordered population demonstrates that most ordered sites belong to one connected region rather than appearing as isolated high-order fluctuations.

At the selected thresholds, 430 of the 510 independently generated cells form the predominantly amorphous population and 80 form the partially ordered comparison population (Fig. 7a,b). The largest-region criterion identifies all 80 partially ordered cells, while the ordered-site criterion identifies a nested subset of 60. Bragg sharpness is non-binding and the archived reference-overlap diagnostic is non-discriminative; both are retained in the Supporting Information as audit quantities rather than treated as coequal determinants of the population. The classification is therefore attributed to connected local order. It measures the extent of crystal-like structure without making the link to a crystallographic phase.

A single threshold choice would conceal how strongly the reported amount of partially ordered material depends on the operational definition. Across the declared 108-setting classifier family, the predominantly amorphous population ranges from 182 to 506 cells, or 35.7%–99.2% of the source population (Fig. 7c). This variation is not evidence for one uniquely correct boundary. It quantifies the range of population assignments supported by the declared family of local-order definitions and makes the resulting uncertainty in the amorphous or partially ordered fraction explicit.

The two populations also differ outside the quantities used to construct the classifier. Their total structure factors retain the broad response of a disordered oxide, but the partially ordered-minus-amorphous difference resolves systematic changes in reciprocal space (Fig. 7d). Together with the real-space pair and angle distributions in Fig. 6, this shows that the population split corresponds to a broader structural change rather than merely to displacement along the classifier coordinates. These correlations are consistent with increased medium-range order, but do not identify a particular crystal structure.

The central result is that in this case the operational order–disorder boundary does not destabilise the dominant local chemistry. At the selected setting, five- and sixfold environments account for 93.72% of Sm sites, while three- and fourfold environments account for 97.90% of O sites (Fig. 7e). Across the complete classifier family, these equal-cell shares vary only from 93.447%–94.055% for Sm and 97.846%–97.943% for O. The number of cells assigned to the amorphous population therefore changes strongly, while the conclusion that a-Sm_2O_3 is dominated

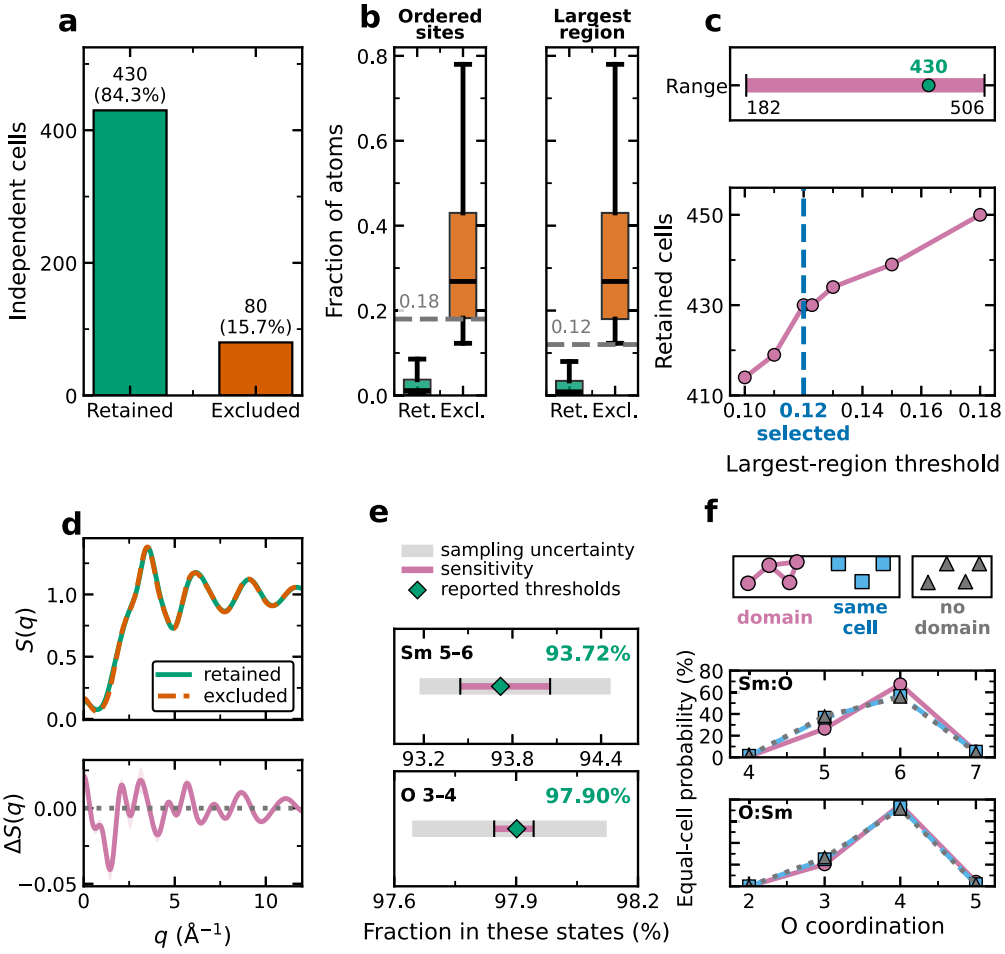


Fig. 7. Crystal-like order and structural robustness in a-Sm_2O_3. (a) Operational split into predominantly amorphous and partially ordered populations. (b) Ordered-site and largest-connected-region fractions with the selected thresholds. (c) Amorphous-population size across the tested threshold family and the largest-region-threshold slice; the selected setting retains 430 cells. (d) Equal-cell total structure factors for the two populations and their difference with 95% uncertainty. (e) Dominant five- and sixfold Sm and three- and fourfold O fractions; grey shows sampling uncertainty, magenta sensitivity and the diamond the selected thresholds. (f) Coordination distributions within connected ordered regions, outside those regions in the same cells and in cells containing no connected ordered region.

by mixed five-/sixfold Sm and three-/fourfold O coordination remains stable.

Connected ordered regions nevertheless select a distinct part of these broad coordination distributions. The Sm population within the ordered region shifts towards sixfold coordination relative to the remainder of the same cell and to cells containing no connected ordered region; the O population shifts correspondingly towards fourfold coordination (Fig. 7f). Equal-cell mean coordinations are 5.776 for Sm and 3.843 for O inside the connected region, compared with 5.658 and 3.771 outside it in the same cells and 5.633 and 3.755 in the no-region population. The supported interpretation is therefore a higher-coordination, crystal-like domain embedded within a disordered mixed-coordinate network, rather than a coordination-idealised phase.

For calculations intended to describe amorphous Sm_2O_3, the partition prevents cells containing extended order from silently biasing ensemble averages. For calculations intended to represent partially crystallised or polycrystalline material, the same ordered-site and connectivity measures provide quantitative descriptors of how much ordered material has formed and whether it is distributed as isolated motifs or connected domains. Crystallographic phase identity would require additional phase-resolved evidence, but the degree and connectivity of crystal-like order are already measurable from the generated population.

The modelling consequence is that population membership and materials inference must be tested separately. The exact number of cells labelled amorphous or partially ordered depends strongly on the selected classifier thresholds, whereas the dominant mixed coordination is robust throughout the declared family. Reporting only the selected 430/80 split would hide the first fact; rejecting the classifier because that split moves would ignore the second. A defensible model should therefore report the operational population definition, its sensitivity and the stability of every downstream structural conclusion.

Reciprocal-space order, pair and angle distributions, classifier prevalence and coordination populations also carry different effective uncertainties under the same set of independent cells. Adding cells generally reduces these uncertainties, but does not define one population size at which all descriptions of Sm_2O_3 become globally converged. Structural distributions and screening descriptors are reported in Figs. S16 and S17; threshold-family sensitivity and classifier-component attribution in Figs. S18 and S19; and descriptor-resolved uncertainty in Fig. S8.

4.5. Systematic modelling of amorphous populations

Together, the three benchmark systems demonstrate a systematic route from ensemble generation to materials-level structural interpretation. In a-SiO_2, conventional pair and angle distributions validate the mean tetrahedral network, while the ring-resolved analysis shows that the lower angular tail is organised by a specific medium-range

topology that is not apparent from the average structure. In a-Si_3N_4, the matched refinement hierarchy separates geometric relaxation from network reconstruction: DFT refinement redistributes density and first-neighbour length scale, sharpens the force-field first shell and repairs marginal contacts, while the PBE and HSE06 descendants retain essentially the same first-neighbour topology. In a-Sm_2O_3, local-order screening quantifies the emergence and connectivity of partially ordered regions from a disordered parent population, while preserving the mixed coordination that characterises the amorphous rare-earth oxide. The three systems therefore resolve complementary aspects of an amorphous ensemble: mean structure, distribution tails, inherited topology and the development of connected order.

Vitriflow makes these distinctions controllable rather than implicit. Calibration defines the preparation-conditioned source population; explicit labels and actions construct the population relevant to the materials question; and cell- or parent-level uncertainty quantifies the precision of each resulting structural statement. Preparation protocols, force fields and refinement methods can consequently be compared without conflating changes in packing, local geometry, network topology or population membership. The result is an auditable connection between what was generated, which structures were analysed and what the sampled population establishes. Quantity-specific uncertainty is reported directly rather than being hidden behind a single assertion of ensemble convergence, while Fig. S20 shows how changes in an operational population definition propagate into the materials result.

5. Conclusions

Structure–property relations in amorphous materials are inherently challenging: they are encoded not only in the mean structure, but in the prevalence, correlations and spatial organisation of local environments across length scales. A model can reproduce density, pair correlations and mean coordination while misrepresenting the strained motifs, distribution tails or connected domains required to capture a material response. The relevant computational object is therefore not a nominal structure, or an ensemble declared globally converged, but a finite population that resolves the property-relevant structural quantity and states the uncertainty with which its prevalence and context are known.

The three materials demonstrate this connection directly. In a-SiO_2, strained bonds and small rings have been implicated in electronic, optical, radiation and chemical responses [99,100]. Here, strain is followed from intra-tetrahedral O–Si–O deformation, through compressed inter-tetrahedral Si–O–Si bridges, to primitive 3-ring topology. The lower angular tail is thereby identified as an organised medium-range population rather than undifferentiated variation about the network mean. In a-Si_3N_4, higher-level refinement is widely used to improve empirically generated structures, but its action on the amorphous network is rarely quantified. The matched hierarchy shows that DFT redistributes density and first-neighbour length scale, sharpens the force-field first shell and repairs marginal contacts, while the PBE and HSE06 descendants retain essentially the same first-neighbour topology. This distinction is central when coordination and connectivity are used to interpret charge trapping, hydrogen response, oxidation and structural transformation [66–69,102]. In Sm_2O_3, where amorphous-to-partially ordered or polycrystalline evolution is relevant to the dielectric and optical behaviour of rare-earth-oxide films [8,9,73], the analysis quantifies both the amount and connectivity of crystal-like order while showing that the mixed coordination characteristic of the disordered oxide remains robust. Structural heterogeneity is thus converted from an uncontrolled feature of the generated cells into a measurable materials variable.

`Vitriflow` makes this analysis executable and auditable within a user-defined parameter space. For newly generated ensembles, it connects a calibrated preparation protocol to the resulting source population; for existing datasets, it begins from the supplied structures and their declared provenance. In either case, it applies the same population construction, screening, structural analysis and uncertainty quantification, records screen labels separately from their actions, and reports the achieved uncertainty of each quantity over its stated sampling unit. Scientific choices remain explicit, but their consequences for population membership, structural resolution and interpretation are measured rather than assumed. The resulting record links how the structures were obtained, which population was analysed and what that finite population establishes, providing a reproducible route from amorphous structure datasets to quantitatively supported structure–property hypotheses.

CRediT authorship contribution statement

Jonathon Cottom: Writing – review & editing, Writing – original draft, Visualization, Validation, Software, Methodology, Investigation, Formal analysis, Data curation, Conceptualization. **Robin Delhomme:** Writing – review & editing, Visualization, Validation, Software, Methodology, Investigation, Formal analysis, Data curation. **Emilia Olsson:** Writing – review & editing, Supervision, Software, Resources, Project administration, Methodology, Funding acquisition, Conceptualization.

Declaration of competing interest

The authors declare that they have no known competing financial interests or personal relationships that could have appeared to influence the work reported in this paper.

Acknowledgements

The authors would like to thank Marsal Colitt Marull, Lina-Henriette Schwering, Xander de Haan, and all members of the Olsson Materials Theory and Modelling group whose assistance has been invaluable in testing and refining `Vitriflow`. This work was conducted at the Advanced Research Center for Nanolithography, a public–private partnership between the University of Amsterdam (UvA), Vrije Universiteit Amsterdam (VU), Rijksuniversiteit Groningen (RUG), the Netherlands Organization for Scientific Research (NWO), and the semiconductor equipment manufacturer ASML. This work made use of the Dutch national e-infrastructure with the support of the SURF Cooperative using grant no. EINF-16595 and EINF-8981. The authors thank SURF (www.surf.nl) for the support in using the National Supercomputer Snellius. This work made use of the ARCNL Minerva cluster hosted at HOPSTER at UvA. E.O. is grateful for a WISE Fellowship from the NWO and acknowledges support via Holland High Tech through a public–private partnership grant in research and development within the Dutch top sector of High-Tech Systems and Materials (HTSM).

Appendix A. Supplementary data

Supplementary material related to this article can be found online at https://doi.org/10.1016/j.commatsci.2026.115098.

Data availability

The `Vitriflow` package is hosted on GitHub (https://github.com/Olsson-Materials-Modelling/Vitriflow); the version specific to this paper is archived in the Zenodo repository [10.5281/zenodo.21111823]. The structures and post-analysis JSON files are freely available in the same Zenodo repository.

References

[1] G.D. Wilk, R.M. Wallace, J.M. Anthony, High-κ gate dielectrics: Current status and materials properties considerations, J. Appl. Phys. 89 (10) (2001) 5243–5275, http://dx.doi.org/10.1063/1.1361065.

[2] J. Robertson, High dielectric constant gate oxides for metal oxide Si transistors, Rep. Progr. Phys. 69 (2) (2006) 327–396, http://dx.doi.org/10.1088/0034-4885/69/2/R02.

[3] T. Kamiya, H. Hosono, Material characteristics and applications of transparent amorphous oxide semiconductors, NPG Asia Mater. 2 (2010) 15–22, http://dx.doi.org/10.1038/asiamat.2010.5.

[4] K. Nomura, H. Ohta, A. Takagi, T. Kamiya, M. Hirano, H. Hosono, Room-temperature fabrication of transparent flexible thin-film transistors using amorphous oxide semiconductors, Nature 432 (7016) (2004) 488–492, http://dx.doi.org/10.1038/nature03090.

[5] C. Xiang, W. Jin, J.E. Bowers, Silicon nitride passive and active photonic integrated circuits: Trends and prospects, Photonics Res. 10 (6) (2022) A82–A96, http://dx.doi.org/10.1364/PRJ.452936.

[6] B.K. Yen, R.L. White, R.J. Waltman, Q. Dai, D.C. Miller, A.J. Kellock, B. Marchon, P.H. Kasai, M.F. Toney, B.R. York, H. Deng, Q.-F. Xiao, V. Raman, Microstructure and properties of ultrathin amorphous silicon nitride protective coating, J. Vac. Sci. Technol. A 21 (6) (2003) 1895–1904, http://dx.doi.org/10.1116/1.1615974.

[7] T.D. Lee, A.U. Ebong, A review of thin film solar cell technologies and challenges, Renew. Sustain. Energy Rev. 70 (2017) 1286–1297, http://dx.doi.org/10.1016/j.rser.2016.12.028.

[8] M. Leskelä, M. Ritala, Rare-earth oxide thin films as gate oxides in MOSFET transistors, J. Solid State Chem. 171 (1–2) (2003) 170–174, http://dx.doi.org/10.1016/S0022-4596(02)00204-9.

[9] A.A. Dakhel, Dielectric and optical properties of samarium oxide thin films, J. Alloys Compd. 365 (1–2) (2004) 233–239, http://dx.doi.org/10.1016/S0925-8388(03)00615-7.

[10] W.H. Zachariasen, The atomic arrangement in glass, J. Am. Chem. Soc. 54 (10) (1932) 3841–3851, http://dx.doi.org/10.1021/ja01349a006.

[11] S.R. Elliott, Medium-range structural order in covalent amorphous solids, Nature 354 (6353) (1991) 445–452, http://dx.doi.org/10.1038/354445a0.

[12] F. Wooten, K. Winer, D. Weaire, Computer generation of structural models of amorphous Si and Ge, Phys. Rev. Lett. 54 (13) (1985) 1392–1395, http://dx.doi.org/10.1103/PhysRevLett.54.1392.

[13] D.S. Franzblau, Computation of ring statistics for network models of solids, Phys. Rev. B 44 (10) (1991) 4925–4930, http://dx.doi.org/10.1103/PhysRevB.44.4925.

[14] H.E. Fischer, A.C. Barnes, P.S. Salmon, Neutron and X-ray diffraction studies of liquids and glasses, Rep. Progr. Phys. 69 (1) (2006) 233–299, http://dx.doi.org/10.1088/0034-4885/69/1/R05.

[15] P.S. Salmon, Real space manifestation of the first sharp diffraction peak in the structure factor of liquid and glassy materials, Proc. R. Soc. Lond. A 445 (1924) (1994) 351–365, http://dx.doi.org/10.1098/rspa.1994.0065.

[16] D.A. Keen, M.T. Dove, Local structures of amorphous and crystalline phases of silica, SiO_2, by neutron total scattering, J. Phys.: Condens. Matter. 11 (47) (1999) 9263–9273, http://dx.doi.org/10.1088/0953-8984/11/47/311.

[17] A. Pedone, Properties calculations of silica-based glasses by atomistic simulations techniques: A review, J. Phys. Chem. C 113 (49) (2009) 20773–20784, http://dx.doi.org/10.1021/jp9071263.

[18] J. Cottom, A. Bochkarev, E. Olsson, K. Patel, M. Munde, J. Spitaler, M.N. Popov, M. Bosman, A.L. Shluger, Modeling of diffusion and incorporation of interstitial oxygen ions at the TiN/SiO_2 interface, ACS Appl. Mater. Interfaces 11 (39) (2019) 36232–36243, http://dx.doi.org/10.1021/acsami.9b10705.

[19] J.K. Christie, Review: understanding the properties of amorphous materials with high-performance computing methods, Philos. Trans. R. Soc. A: Math. Phys. Eng. Sci. 381 (2250) (2023) 20220251, http://dx.doi.org/10.1098/rsta.2022.0251.

[20] A. Madanchi, E. Azek, K. Zongo, L.K. Béland, N. Mousseau, L. Simine, Is the future of materials amorphous? Challenges and opportunities in simulations of amorphous materials, ACS Phys. Chem. Au 5 (1) (2025) 3–16, http://dx.doi.org/10.1021/acsphyschemau.4c00063.

[21] H. Liu, Z. Zhao, Q. Zhou, R. Chen, K. Yang, Z. Wang, L. Tang, M. Bauchy, Challenges and opportunities in atomistic simulations of glasses: A review, Comptes Rendus Géosci. 354 (S1) (2022) 35–77, http://dx.doi.org/10.5802/crgeos.116.

[22] C. Massobrio, J. Du, M. Bernasconi, P.S. Salmon (Eds.), Molecular Dynamics Simulations of Disordered Materials, in: Springer Series in Materials Science, vol. 215, Springer, Cham, 2015, http://dx.doi.org/10.1007/978-3-319-15675-0.

[23] A.C. Wright, The comparison of molecular dynamics simulations with diffraction experiments, J. Non-Cryst. Solids 159 (3) (1993) 264–268, http://dx.doi.org/10.1016/0022-3093(93)90232-M.

[24] R. Car, M. Parrinello, Unified approach for molecular dynamics and density-functional theory, Phys. Rev. Lett. 55 (22) (1985) 2471–2474, http://dx.doi.org/10.1103/PhysRevLett.55.2471.

[25] B.W.H. van Beest, G.J. Kramer, R.A. van Santen, Force fields for silicas and aluminophosphates based on ab initio calculations, Phys. Rev. Lett. 64 (16) (1990) 1955–1958, http://dx.doi.org/10.1103/PhysRevLett.64.1955.

[26] J. Behler, M. Parrinello, Generalized neural-network representation of high-dimensional potential-energy surfaces, Phys. Rev. Lett. 98 (14) (2007) 146401, http://dx.doi.org/10.1103/PhysRevLett.98.146401.

[27] A.P. Bartók, M.C. Payne, R. Kondor, G. Csányi, Gaussian approximation potentials: The accuracy of quantum mechanics, without the electrons, Phys. Rev. Lett. 104 (13) (2010) 136403, http://dx.doi.org/10.1103/PhysRevLett.104.136403.

[28] J. Behler, Perspective: Machine learning potentials for atomistic simulations, J. Chem. Phys. 145 (17) (2016) 170901, http://dx.doi.org/10.1063/1.4966192.

[29] O.T. Unke, S. Chmiela, H.E. Sauceda, M. Gastegger, I. Poltavsky, K.T. Schütt, A. Tkatchenko, K.-R. Müller, Machine learning force fields, Chem. Rev. 121 (16) (2021) 10142–10186, http://dx.doi.org/10.1021/acs.chemrev.0c01111.

[30] V.L. Deringer, N. Bernstein, A.P. Bartók, M.J. Cliffe, R.N. Kerber, L.E. Marbella, C.P. Grey, S.R. Elliott, G. Csányi, Realistic atomistic structure of amorphous silicon from machine-learning-driven molecular dynamics, J. Phys. Chem. Lett. 9 (11) (2018) 2879–2885, http://dx.doi.org/10.1021/acs.jpclett.8b00902.

[31] K. Vollmayr, W. Kob, K. Binder, Cooling-rate effects in amorphous silica: A computer-simulation study, Phys. Rev. B 54 (22) (1996) 15808–15827, http://dx.doi.org/10.1103/PhysRevB.54.15808.

[32] J. Horbach, W. Kob, Static and dynamic properties of a viscous silica melt, Phys. Rev. B 60 (5) (1999) 3169–3181, http://dx.doi.org/10.1103/PhysRevB.60.3169.

[33] J.M.D. Lane, Cooling rate and stress relaxation in silica melts and glasses via microsecond molecular dynamics, Phys. Rev. E 92 (1) (2015) 012320, http://dx.doi.org/10.1103/PhysRevE.92.012320.

[34] A. Nakano, R.K. Kalia, P. Vashishta, First sharp diffraction peak and intermediate-range order in amorphous silica: Finite-size effects in molecular dynamics simulations, J. Non-Cryst. Solids 171 (2) (1994) 157–163, http://dx.doi.org/10.1016/0022-3093(94)90351-4.

[35] S. von Alfthan, A. Kuronen, K. Kaski, Realistic models of amorphous silica: A comparative study of different potentials, Phys. Rev. B 68 (7) (2003) 073203, http://dx.doi.org/10.1103/PhysRevB.68.073203.

[36] T. Uchino, J.D. Harrop, S.N. Taraskin, S.R. Elliott, Real and reciprocal space structural correlations contributing to the first sharp diffraction peak in silica glass, Phys. Rev. B 71 (1) (2005) 014202, http://dx.doi.org/10.1103/PhysRevB.71.014202.

[37] S. Sundararaman, L. Huang, S. Ispas, W. Kob, New optimization scheme to obtain interaction potentials for oxide glasses, J. Chem. Phys. 148 (19) (2018) 194504, http://dx.doi.org/10.1063/1.5023707.

[38] M. Ippolito, S. Meloni, Atomistic structure of amorphous silicon nitride from classical molecular dynamics simulations, Phys. Rev. B 83 (16) (2011) 165209, http://dx.doi.org/10.1103/PhysRevB.83.165209.

[39] A. Dasmahapatra, P. Kroll, Modeling amorphous silicon nitride: A comparative study of empirical potentials, Comput. Mater. Sci. 148 (2018) 165–175, http://dx.doi.org/10.1016/j.commatsci.2017.12.008.

[40] F. de Brito Mota, J.F. Justo, A. Fazzio, Structural properties of amorphous silicon nitride, Phys. Rev. B 58 (13) (1998) 8323–8328, http://dx.doi.org/10.1103/PhysRevB.58.8323.

[41] C.M. Marian, M. Gastreich, J.D. Gale, Empirical two-body potential for solid silicon nitride, boron nitride, and borosilazane modifications, Phys. Rev. B 62 (5) (2000) 3117–3124, http://dx.doi.org/10.1103/PhysRevB.62.3117.

[42] I. Štich, R. Car, M. Parrinello, Amorphous silicon studied by ab initio molecular dynamics: Preparation, structure, and properties, Phys. Rev. B 44 (20) (1991) 11092–11104, http://dx.doi.org/10.1103/PhysRevB.44.11092.

[43] M.D. Kluge, J.R. Ray, Amorphous-silicon formation by rapid quenching: A molecular-dynamics study, Phys. Rev. B 36 (8) (1987) 4234–4237, http://dx.doi.org/10.1103/PhysRevB.36.4234.

[44] M. Ishimaru, S. Munetoh, T. Motooka, Generation of amorphous silicon structures by rapid quenching: A molecular-dynamics study, Phys. Rev. B 56 (23) (1997) 15133–15138, http://dx.doi.org/10.1103/PhysRevB.56.15133.

[45] W. Li, Y. Ando, Dependence of a cooling rate on structural and vibrational properties of amorphous silicon: A neural network potential-based molecular dynamics study, J. Chem. Phys. 151 (11) (2019) 114101, http://dx.doi.org/10.1063/1.5114652.

[46] I. Santos, M. Aboy, L.A. Marqués, P. López, L. Pelaz, Generation of amorphous Si structurally compatible with experimental samples through the quenching process: A systematic molecular dynamics simulation study, J. Non-Cryst. Solids 503–504 (2019) 20–27, http://dx.doi.org/10.1016/j.jnoncrysol.2018.09.024.

[47] S. Nosé, A unified formulation of the constant temperature molecular dynamics methods, J. Chem. Phys. 81 (1) (1984) 511–519, http://dx.doi.org/10.1063/1.447334.

[48] W.G. Hoover, Canonical dynamics: Equilibrium phase-space distributions, Phys. Rev. A 31 (3) (1985) 1695–1697, http://dx.doi.org/10.1103/PhysRevA.31.1695.

[49] G.J. Martyna, D.J. Tobias, M.L. Klein, Constant pressure molecular dynamics algorithms, J. Chem. Phys. 101 (5) (1994) 4177–4189, http://dx.doi.org/10.1063/1.467468.

[50] J.E. Basconi, M.R. Shirts, Effects of temperature control algorithms on transport properties and kinetics in molecular dynamics simulations, J. Chem. Theory Comput. 9 (7) (2013) 2887–2899, http://dx.doi.org/10.1021/ct400109a.

[51] S.C. Harvey, R.K.-Z. Tan, T.E. Cheatham III, The flying ice cube: Velocity rescaling in molecular dynamics leads to violation of energy equipartition, J. Comput. Chem. 19 (7) (1998) 726–740, http://dx.doi.org/10.1002/(SICI)1096-987X(199805)19:7<726::AID-JCC4>3.0.CO;2-S.

[52] E. Braun, S.M. Moosavi, B. Smit, Anomalous effects of velocity rescaling algorithms: The flying ice cube effect revisited, J. Chem. Theory Comput. 14 (10) (2018) 5262–5272, http://dx.doi.org/10.1021/acs.jctc.8b00446.

[53] H. Kim, B. Fábián, G. Hummer, Neighbor list artifacts in molecular dynamics simulations, J. Chem. Theory Comput. 19 (23) (2023) 8919–8929, http://dx.doi.org/10.1021/acs.jctc.3c00777.

[54] M.W. Thompson, J.B. Gilmer, R.A. Matsumoto, C.D. Quach, P. Shamaprasad, A.H. Yang, C.R. Iacovella, C. McCabe, P.T. Cummings, Towards molecular simulations that are transparent, reproducible, usable by others, and extensible (TRUE), Mol. Phys. 118 (9–10) (2020) e1742938, http://dx.doi.org/10.1080/00268976.2020.1742938.

[55] G. Pizzi, A. Cepellotti, R. Sabatini, N. Marzari, B. Kozinsky, AiiDA: Automated interactive infrastructure and database for computational science, Comput. Mater. Sci. 111 (2016) 218–230, http://dx.doi.org/10.1016/j.commatsci.2015.09.013.

[56] M. Uhrin, S.P. Huber, J. Yu, N. Marzari, G. Pizzi, Workflows in AiiDA: Engineering a high-throughput, event-based engine for robust and modular computational workflows, Comput. Mater. Sci. 187 (2021) 110086, http://dx.doi.org/10.1016/j.commatsci.2020.110086.

[57] A. Jain, S.P. Ong, W. Chen, B. Medasani, X. Qu, M. Kocher, M. Brafman, G. Petretto, G.-M. Rignanese, G. Hautier, D. Gunter, K.A. Persson, FireWorks: A dynamic workflow system designed for high-throughput applications, Concurr. Comput.: Pr. Exp. 27 (17) (2015) 5037–5059, http://dx.doi.org/10.1002/cpe.3505.

[58] K. Mathew, J.H. Montoya, A. Faghaninia, S. Dwarakanath, M. Aykol, H. Tang, I.-h. Chu, T. Smidt, B. Bocklund, M. Horton, J. Dagdelen, B. Wood, Z.-K. Liu, J. Neaton, S.P. Ong, K. Persson, A. Jain, Atomate: A high-level interface to generate, execute, and analyze computational materials science workflows, Comput. Mater. Sci. 139 (2017) 140–152, http://dx.doi.org/10.1016/j.commatsci.2017.07.030.

[59] C.S. Adorf, P.M. Dodd, V. Ramasubramani, S.C. Glotzer, Simple data and workflow management with the signac framework, Comput. Mater. Sci. 146 (2018) 220–229, http://dx.doi.org/10.1016/j.commatsci.2018.01.035.

[60] J. Janssen, S. Surendralal, Y. Lysogorskiy, M. Todorova, T. Hickel, R. Drautz, J. Neugebauer, Pyiron: An integrated development environment for computational materials science, Comput. Mater. Sci. 163 (2019) 24–36, http://dx.doi.org/10.1016/j.commatsci.2018.07.043.

[61] I. Batatia, P. Benner, Y. Chiang, A.M. Elena, D.P. Kovács, et al., A foundation model for atomistic materials chemistry, J. Chem. Phys. 163 (18) (2025) 184110, http://dx.doi.org/10.1063/5.0297006.

[62] E. Kasoar, J. Hart, I. Batatia, G. Csányi, A.M. Elena, ML-PEG (machine learning performance and extrapolation guide) GitHubref Repository, 2025, URL https://resources.psdi.ac.uk/tool/1a4047ca-1994-4fcc-876f-abd9ab43d937. Physical Sciences Data Infrastructure online resource, version 0.3.1, 3 April 2025.

[63] K. Yang, D. Schwalbe-Koda, A generative diffusion model for amorphous materials, Npj Comput. Mater. 12 (2026) 29, http://dx.doi.org/10.1038/s41524-025-01901-1.

[64] J.A. Finkler, Y. Lin, T. Du, J. Hu, M.M. Smedskjaer, Inverse design of amorphous materials with targeted properties, Adv. Mater. 38 (39) (2026) e22493, http://dx.doi.org/10.1002/adma.202522493.

[65] K. Patel, J. Cottom, A. Mehonic, W.H. Ng, A.J. Kenyon, M. Bosman, A.L. Shluger, The nature of column boundaries in micro-structured silicon oxide nanolayers, APL Mater. 9 (12) (2021) 121107, http://dx.doi.org/10.1063/5.0073349.

[66] L. Hückmann, J. Cottom, J. Meyer, Intrinsic charge trapping and reversible charge induced structural modifications in a-Si_3N_4, Adv. Phys. Res. 3 (2) (2024) 2300109, http://dx.doi.org/10.1002/apxr.202300109.

[67] J. Cottom, L. Hückmann, E. Olsson, J. Meyer, From Jekyll to Hyde and beyond: Hydrogen's multifaceted role in passivation, H-induced breakdown, and charging of amorphous silicon nitride, J. Phys. Chem. Lett. 15 (3) (2024) 840–848, http://dx.doi.org/10.1021/acs.jpclett.3c03376.

[68] L. Hückmann, R. Sylvia, F. Blankenvoorde, J. Cottom, J. Meyer, Mechanistic insights into the dry oxidation of amorphous silicon nitride: A DFT study, J. Mater. Chem. C 14 (1) (2026) 139–151, http://dx.doi.org/10.1039/D5TC03484A.

[69] J. Cottom, L. Hückmann, J. Meyer, E. Olsson, Forged by charge: Polaron-induced matrix formation in silicon nitride conversion-type anodes for lithium-ion batteries, J. Mater. Chem. A 13 (40) (2025) 34260–34272, http://dx.doi.org/10.1039/D5TA04013B.

[70] V.L. Deringer, Modelling and understanding battery materials with machine-learning-driven atomistic simulations, J. Phys.: Energy 2 (4) (2020) 041003, http://dx.doi.org/10.1088/2515-7655/abb011.

[71] K. Konstantinou, F.C. Mocanu, T.-H. Lee, S.R. Elliott, Revealing the intrinsic nature of the mid-gap defects in amorphous $Ge_2Sb_2Te_5$, Nat. Commun. 10 (1) (2019) 3065, http://dx.doi.org/10.1038/s41467-019-10980-w.

[72] K. Konstantinou, S.R. Elliott, J. Akola, Inherent electron and hole trapping in amorphous phase-change memory materials: $Ge_2Sb_2Te_5$, J. Mater. Chem. C 10 (17) (2022) 6744–6753, http://dx.doi.org/10.1039/D2TC00486K.

[73] E. Olsson, Q. Cai, J. Cottom, R. Jakobsen, A.L. Shluger, Structural, elastic, vibrational and electronic properties of amorphous Sm_2O_3 from Ab initio calculations, Comput. Mater. Sci. 169 (2019) 109119, http://dx.doi.org/10.1016/j.commatsci.2019.109119.

[74] S. Plimpton, Fast parallel algorithms for short-range molecular dynamics, J. Comput. Phys. 117 (1) (1995) 1–19, http://dx.doi.org/10.1006/jcph.1995.1039.

[75] A.P. Thompson, H.M. Aktulga, R. Berger, D.S. Bolintineanu, W.M. Brown, P.S. Crozier, P.J. in 't Veld, A. Kohlmeyer, S.G. Moore, T.D. Nguyen, R. Shan, M.J. Stevens, J. Tranchida, C. Trott, S.J. Plimpton, LAMMPS – a flexible simulation tool for particle-based materials modeling at the atomic, meso, and continuum scales, Comput. Phys. Comm. 271 (2022) 108171, http://dx.doi.org/10.1016/j.cpc.2021.108171.

[76] M.D. Hanwell, K.M. Martin, A. Chaudhary, L.S. Avila, The visualization toolkit (VTK): Rewriting the rendering code for modern graphics cards, SoftwareX 1–2 (2015) 9–12, http://dx.doi.org/10.1016/j.softx.2015.04.001.

[77] J.D. Hunter, Matplotlib: A 2D graphics environment, Comput. Sci. Eng. 9 (3) (2007) 90–95, http://dx.doi.org/10.1109/MCSE.2007.55.

[78] M. Parrinello, A. Rahman, Crystal structure and pair potentials: A molecular-dynamics study, Phys. Rev. Lett. 45 (14) (1980) 1196–1199, http://dx.doi.org/10.1103/PhysRevLett.45.1196.

[79] E. Olsson, X. Aparicio-Anglès, N.H. de Leeuw, A computational study of the electronic properties, ionic conduction, and thermal expansion of $Sm_{1-x}A_xCoO_3$ and $Sm_{1-x}A_xCoO_{3-x/2}$ (A=Ba^{2+}, Ca^{2+}, Sr^{2+}, and x=0.25, 0.5) as intermediate temperature SOFC cathodes, Phys. Chem. Chem. Phys. 19 (2017) 13960–13969, http://dx.doi.org/10.1039/C7CP01555K.

[80] R.A. Buckingham, The classical equation of state of gaseous helium, neon and argon, Proc. R. Soc. Lond. A 168 (933) (1938) 264–283, http://dx.doi.org/10.1098/rspa.1938.0173.

[81] J.F. Ziegler, J.P. Biersack, U. Littmark, The Stopping and Range of Ions in Solids, Pergamon Press, New York, 1985.

[82] T.D. Kühne, M. Iannuzzi, M. Del Ben, V.V. Rybkin, P. Seewald, F. Stein, T. Laino, R.Z. Khaliullin, O. Schütt, F. Schiffmann, D. Golze, J. Wilhelm, S. Chulkov, M.H. Bani-Hashemian, V. Weber, U. Borštnik, M. Taillefumier, A.S. Jakobovits, A. Lazzaro, H. Pabst, T. Müller, R. Schade, M. Guidon, S. Andermatt, N. Holmberg, G.K. Schenter, A. Hehn, A. Bussy, F. Belleflamme, G. Tabacchi, A. Glöß, M. Lass, I. Bethune, C.J. Mundy, C. Plessl, M. Watkins, J. VandeVondele, M. Krack, J. Hutter, CP2K: An electronic structure and molecular dynamics software package – Quickstep: Efficient and accurate electronic structure calculations, J. Chem. Phys. 152 (19) (2020) 194103, http://dx.doi.org/10.1063/5.0007045.

[83] J. VandeVondele, M. Krack, F. Mohamed, M. Parrinello, T. Chassaing, J. Hutter, Quickstep: Fast and accurate density functional calculations using a mixed Gaussian and plane waves approach, Comput. Phys. Comm. 167 (2) (2005) 103–128, http://dx.doi.org/10.1016/j.cpc.2004.12.014.

[84] J.P. Perdew, K. Burke, M. Ernzerhof, Generalized gradient approximation made simple, Phys. Rev. Lett. 77 (18) (1996) 3865–3868, http://dx.doi.org/10.1103/PhysRevLett.77.3865.

[85] J. Heyd, G.E. Scuseria, M. Ernzerhof, Hybrid functionals based on a screened Coulomb potential, J. Chem. Phys. 118 (18) (2003) 8207–8215, http://dx.doi.org/10.1063/1.1564060.

[86] J. Heyd, G.E. Scuseria, M. Ernzerhof, Erratum: "hybrid functionals based on a screened Coulomb potential" [J. Chem. Phys. **118**, 8207 (2003)], J. Chem. Phys. 124 (21) (2006) 219906, http://dx.doi.org/10.1063/1.2204597.

[87] A.V. Krukau, O.A. Vydrov, A.F. Izmaylov, G.E. Scuseria, Influence of the exchange screening parameter on the performance of screened hybrid functionals, J. Chem. Phys. 125 (22) (2006) 224106, http://dx.doi.org/10.1063/1.2404663.

[88] M. Guidon, J. Hutter, J. VandeVondele, Auxiliary density matrix methods for Hartree-Fock exchange calculations, J. Chem. Theory Comput. 6 (8) (2010) 2348–2364, http://dx.doi.org/10.1021/ct1002225.

[89] J. VandeVondele, J. Hutter, Gaussian basis sets for accurate calculations on molecular systems in gas and condensed phases, J. Chem. Phys. 127 (11) (2007) 114105, http://dx.doi.org/10.1063/1.2770708.

[90] S. Goedecker, M. Teter, J. Hutter, Separable dual-space Gaussian pseudopotentials, Phys. Rev. B 54 (3) (1996) 1703–1710, http://dx.doi.org/10.1103/PhysRevB.54.1703.

[91] C. Hartwigsen, S. Goedecker, J. Hutter, Relativistic separable dual-space Gaussian pseudopotentials from H to Rn, Phys. Rev. B 58 (7) (1998) 3641–3662, http://dx.doi.org/10.1103/PhysRevB.58.3641.

[92] M. Krack, Pseudopotentials for H to Kr optimized for gradient-corrected exchange-correlation functionals, Theor. Chem. Acc. 114 (1–3) (2005) 145–152, http://dx.doi.org/10.1007/s00214-005-0655-y.

[93] C.G. Broyden, The convergence of a class of double-rank minimization algorithms 2. the new algorithm, IMA J. Appl. Math. 6 (3) (1970) 222–231, http://dx.doi.org/10.1093/imamat/6.3.222.

[94] R. Fletcher, A new approach to variable metric algorithms, Comput. J. 13 (3) (1970) 317–322, http://dx.doi.org/10.1093/comjnl/13.3.317.
[95] D. Goldfarb, A family of variable-metric methods derived by variational means, Math. Comp. 24 (109) (1970) 23–26, http://dx.doi.org/10.1090/S0025-5718-1970-0258249-6.
[96] D.F. Shanno, Conditioning of Quasi-Newton methods for function minimization, Math. Comp. 24 (111) (1970) 647–656, http://dx.doi.org/10.1090/S0025-5718-1970-0274029-X.
[97] P.J. Steinhardt, D.R. Nelson, M. Ronchetti, Bond-orientational order in liquids and glasses, Phys. Rev. B 28 (2) (1983) 784–805, http://dx.doi.org/10.1103/PhysRevB.28.784.
[98] W. Lechner, C. Dellago, Accurate determination of crystal structures based on averaged local bond order parameters, J. Chem. Phys. 129 (11) (2008) 114707, http://dx.doi.org/10.1063/1.2977970.
[99] T. Uchino, Y. Kitagawa, T. Yoko, Structure, energies, and vibrational properties of silica rings in SiO_2 glass, Phys. Rev. B 61 (1) (2000) 234–240, http://dx.doi.org/10.1103/PhysRevB.61.234.
[100] K. Awazu, H. Kawazoe, Strained Si–O–Si bonds in amorphous SiO_2 materials: A family member of active centers in radio, photo, and chemical responses, J. Appl. Phys. 94 (10) (2003) 6243–6262, http://dx.doi.org/10.1063/1.1618351.
[101] F. Mauri, A. Pasquarello, B.G. Pfrommer, Y.-G. Yoon, S.G. Louie, Si–O–Si bond-angle distribution in vitreous silica from first-principles ^{29}Si NMR analysis, Phys. Rev. B 62 (8) (2000) R4786–R4789, http://dx.doi.org/10.1103/PhysRevB.62.R4786.
[102] C. Wilhelmer, L. Hückmann, J. Cottom, D. Waldhoer, J. Meyer, T. Grasser, Microscopic origins of electron trapping in amorphous silicon nitride (a-Si_3N_4) and its role in charge-trap flash memory, J. Phys.: Condens. Matter. 38 (33) (2026) 333002, http://dx.doi.org/10.1088/1361-648X/ae8b4d.